Band-Gap Engineering of Mo- and W-Containing Perovskite Oxides Derived from Barium Titanate

Or Shafir⬤, Alexey Shopin, and Ilya Grinberg[*]
Department of Chemistry, Bar-Ilan University, Ramat Gan, Israel

Ferroelectric oxide perovskites are promising materials for use in photovoltaic devices, due to their ability to exploit the bulk photovoltaic effect to achieve high power-conversion efficiency. In this work, we use first-principles methods to investigate the ferroelectric perovskite $[BaTiO_3]_x$-$[NaTi_{1/2}Mo_{1/2}O_3]_{1-x}$ and $[BaTiO_3]_x$-$[NaTi_{1/2}W_{1/2}O_3]_{1-x}$ solid solutions for potential use in ferroelectric-based photovoltaics. We find that compositional variations change the band gap, shifting it to the edge of the visible range for the 25% $NaTi_{1/2}Mo_{1/2}O_3$ composition and to the visible range for some Mo-cation and W-cation arrangements for the 50% $NaTi_{1/2}Mo_{1/2}O_3$ and 50% $NaTi_{1/2}W_{1/2}O_3$ compositions. Mo and W substitutions both maintain the ferroelectric properties of the parent $BaTiO_3$. While the A-site cation arrangement has a minor effect on the band gap, the variations in the B-site cation arrangement and the cation displacements affect the band gap by up to 0.8 eV. Analysis of the structures and the calculated band-gap values shows that the band gap is controlled by the identity of the substituent cation, the O-B-O angles, the relative orientations of the Mo and W substituent atoms, and the B-cation displacement. We demonstrate the thermodynamic feasibility of these solid solutions by formation energy analysis. The decrease of the band gap relative to the parent $BaTiO_3$ to the standard and transparent photovoltaic range combined with the ferroelectricity maintained make this earth-abundant-containing solid solution a promising candidate for use in high-performance ferroelectric-based photovoltaic devices.

I. INTRODUCTION

Because of an inexhaustible supply of energy from the Sun and the lack of emissions, conversion of sunlight into electricity by photovoltaics (PVs) is the most-promising long-term sustainable-energy technology. Recent experimental and theoretical work has shown that ferroelectric (FE) oxides may be a new promising candidate class of materials for PV applications due to the bulk photovoltaic effect (BPVE), which in principle can enable power-conversion efficiency (PCE) beyond the Shockley-Queiser limit [1–6]. In addition, because of their polar nature, FE-based devices do not require a p-n junction for excited-charge-carrier separation [3,7]. Several studies demonstrated that a low band gap (E_g) and large polarization (P) can be combined in FE oxides and elucidated the relationships between the composition and structure of the oxide and its E_g, motivating the ongoing exploration of perovskite solid-solution FEs for visible-light absorption [8–13].

The BPVE is observed for noncentrosymmetric crystals such as FE oxide perovskites and gives rise to photovoltages larger than the band gap. The ballistic photocurrent

mechanism is one of the mechanisms of BPVE, and is the origin of the high photocurrent recently observed in nanoscale FE PV devices [1]. In this case, the photocurrent is generated by nonthermalized charge carriers, which travel ballistically in a preferred direction. The direction preference is due to the asymmetry of the polar crystal, which gives rise to an asymmetric momentum distribution for a short time, until the decay of the charge carriers to the conduction band. The decay to the conduction band occurs over a certain material-specific distance known as the "thermalization length" that has been estimated to be on the order of 100 nm for $BaTiO_3$ [1,7]. Since only the photocarriers generated at the surface layer with depth equal to the thermalization length contribute to the ballistic photocurrent, all FE PV devices relying on this mechanism act as thin films and the use of thicker film to maximize light absorption will not result in a higher photocurrent, unlike in the traditional p-n-junction-based PV devices. Therefore, for practical application, the FE PV material must exhibit strong light absorption that enables the collection of solar energy over a short distance (approximately 100 nm). This means that to enable FE PV devices with a high PCE, the FE solar absorber must have a direct band gap with a dipole-allowed across-the-band-gap excitation transition.

[*]ilya.grinberg@biu.ac.il

For FE PV devices, large P is necessary for the following reasons. First, it allows a high PCE to be achieved and enables the practical application of FE PV devices. According to the phenomenological theory of the ballistic current BPVE, the photocurrent generated due to the intrinsic asymmetry of the bulk FE material is proportional to P^2 [14]. In addition, a large P also favors the screening-derived enhancement of the local electric field, which is believed to play a key role in the PCE beyond the Shockley-Queiser limit obtained by use of FE PV devices with nanoscale electrodes [1]. Finally, a large P favors a high T_C of the material [15,16], which is necessary for the stability of the polarization at high operational temperatures generated by intense light illumination.

While many studies have explored visible-light-absorbing FEs in the past decade, many of these have focused on the achievement of visible-light absorption through the inclusion of vacancies and non-d^0 transition metals. This approach can efficiently lower the band gap of the FE material but often either leads to a decreased polarization or uses a dipole-forbidden d-d across-the-band-gap transition that prevents the strong absorption of light in a thin film with thickness equal to the thermalization length. To enable strong light absorption necessary for practical FE PV devices, a d^0-configuration B-site cation should be used to utilize the dipole allowed O $2p$–to–B d transition. Additionally, the d^0 configuration and large P are linked in perovskite oxides, since a d^0 B site is necessary for the polarization-generating second-order Jahn-Teller effect. However, while the d^0 B site is favorable for obtaining strong light absorption and large P, because of the high electronegativity difference between O and the d^0 transition metal, the d^0 B site is typically accompanied by a larger E_g compared with the perovskite oxides with a non-d^0 metal. Such large band gaps prevent efficient light absorption and the realization of high PCE.

Ferroelectric-based PVs may be particularly important for transparent photovoltaics, since in this case, the lack of use of the visible-light range of the solar spectrum necessitates the maximum use of the high-energy part of the spectrum for photon energies greater than approximately 2.8 eV. Here, the possible overcoming of the Shockley-Queiser limit by the BPVE-based FE device is particularly promising. Here, as well, a material with a direct O $2p$–to–B d band gap of 2.8 eV (or slightly below) and large P will be necessary to enable practical transparent FE-based PV devices. Finally, for both visible-light-absorbing and visible-light-transparent PVs, the absorber material should consist of Earth-abundant, inexpensive, and nontoxic elements.

Therefore, to obtain FE PV materials that can simultaneously exhibit a d^0 B-site configuration and visible-light absorption, using first-principles calculations, we explore the band engineering of FE perovskite oxides to obtain

candidate materials for FE PVs by substitution of d^0-configuration Mo^{6+} and W^{6+} cations into the classic $BaTiO_3$ (BTO) FE so as to obtain materials with a high P but lower E_g than that of the parent $BaTiO_3$ material. Previous studies demonstrated that the properties of $BaTiO_3$ can be tuned by combination in in solid solutions [17–19], and that the band gap of parent $BaTiO_3$ can be decreased by doping or combination in a solid solution [2,20–22]. Such solid solutions and doped $BaTiO_3$ materials showed enhanced PV performance [19,22]. An experimental study of Mo-doped $BaTiO_3$ demonstrated an E_g decrease [23], and increased hole mobility was found in a theoretical study [24].

We expect that lower E_g will be obtained in Mo^{6+}-doped and W^{6+}-doped $BaTiO_3$ due to the higher electronegativity of Mo^{6+} and W^{6+} compared with Ti^{4+} of $BaTiO_3$ [25]. Since the across-the-band-gap excitation in ABO_3 materials is essentially a charge transfer from the oxygen to the B-site cation [26], the higher electronegativity of Mo^{6+} and W^{6+} should lead to lower E_g. Since the O $2p$–to–Mo $4d$ and O $2p$–to–W $5d$ transitions are dipole allowed, we expect that the materials obtained will absorb light strongly, which is favorable for their use as thin-film absorbers. We expect the binding energy to be small for this material, since the O $2p$ states of the valence band relate to the oxygen's nonbonding electrons. Additionally, previous work demonstrated that on Mo doping in $BaTiO_3$, the binding energy decreased [23]. For charge balance, a substitution of each Mo or W atom at the B site is accompanied by the substitution of two Na atoms at the A site. Thus, the materials obtained can be thought of as $[BaTiO_3]_x$-$[NaTi_{1/2}Mo_{1/2}O_3]_{1-x}$ (BTO-NTM) and $[BaTiO_3]_x$-$[NaTi_{1/2}W_{1/2}O_3]_{1-x}$ (BTO-NTW) solid solutions. Since these solid solutions contain only ferroelectrically active cations at the B site, they are expected to preserve or even enhance the polarization of the parent $BaTiO_3$ material, which will be favorable for the FE stability of these solid solutions at room temperature.

We focus on composition ratios of $x = 0.75$ and $x = 0.5$, which we refer to as 75BTO-25NTM and 50BTO-50NTM, respectively, for the Mo-containing solid solutions or 75BTO-25NTW and 50BTO-50NTW, respectively, for the W-containing solid solutions. Using first-principles calculations, we show how the changes of the phase, the local structure, and the substituent content affect E_g and P of the material and demonstrate that 75BTO-25NTM exhibits the desired combination of P and lower E_g suitable for the transparency requirement [27] of E_g greater than 2.85 eV (the edge of the visible spectrum), and is likely to be promising for use in transparent FE-based PV devices. The increased P of 75BTO-25NTM makes it likely that it will exhibit greater temperature stability and stronger ballistic photocurrent than $BaTiO_3$ and may be promising for applications of transparent photovoltaics utilizing the

PCE beyond the Shockley-Queiser limit enabled by hot-carrier FE-based PVs. Additionally, all of the constituent elements of 75BTO-25NTM are Earth abundant and non-toxic, which is favorable for the practical applications of devices based on this material.

II. METHODS

A. Supercell design

To study how the substitution in BTO-NTM and BTO-NTW changes the properties of BaTiO$_3$, we use $2 \times 2 \times 2$ 40-atom supercells and perform calculations for compositions with 75% and 50% BaTiO$_3$ content. For each composition, several cation arrangements are studied. For 75BTO-25NTM and 75BTO-25NTW, we study different Na substitution arrangements, which are referred to as $(100)_A$, $(110)_A$, and $(111)_A$, denoting the Na-replacement orientation (with A referring to the A site). For 50BTO-50NTM and 50BTO-50NTW, we study the arrangements $(100)_A(100)_B$, $(100)_A(110)_B$, $(111)_A(110)_B$, and $(111)_A(111)_B$, with A indicating the Na and Ba stacking orientation and B indicating the orientation of the Mo or W replaced sites (Fig. 1). To explore the potential-energy surface (PES), we impose initial displacements of the cations in the x, z, x-y, and x-y-z directions and then fully relax the energy with respect to ionic coordinates and lattice parameters. In many cases, all relaxations found the same ground state, but in some cases multiple PES minima were found. Table I summarizes the compositions, arrangements, and displacements studied.

B. Computational methods

All relaxations are performed with the QUANTUM ESPRESSO package [28], using the pseudopotentials from the GBRV pseudopotential database [29] to represent the effect of the nuclei and the core electrons on the valence electrons. All relaxations are performed with the local-density approximation (LDA) [30] of Perdew and Zunger
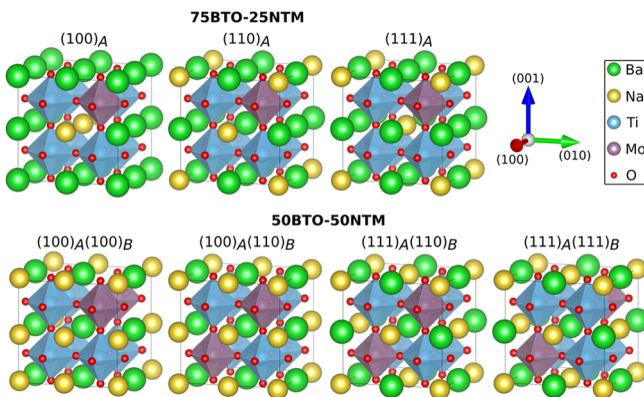
[31] for the exchange-correlation functional. P is calculated using the Berry-phase method [32] as implemented in QUANTUM ESPRESSO. The LDA is known to underestimate the volume of BaTiO$_3$ and other perovskites, leading to underestimation of P [33]. Thus, it provides a lower-limit estimate for the experimental P. The LDA is well known to obtain lower E_g values than experiments [33]. Therefore, E_g calculations are performed for the relaxed structures both with QUANTUM ESPRESSO and with the all-electron FHI-aims code [34]. LDA E_g values are calculated with QUANTUM ESPRESSO, and HSE06 hybrid exchange-correlation functional calculations are performed with FHI-aims.

The electronic structure is evaluated along the Γ (0,0,0)–X (0.5,0.0,0.0)–M (0.5,0.5,0)–Γ (0,0,0)–R (0.5,0.5,0.5)–M (0.5,0.5,0) path in the Brillouin zone. Comparison of the LDA and HSE06 E_g values for the structures studied shows that the HSE06 values can be obtained by an essentially rigid shift of the LDA E_g values by 1.29 eV ($E_g^{\text{HSE06}} = E_g^{\text{LDA}} + 1.29$ eV) and comparison of the HSE06 and experimental E_g values shows that the HSE06 values are very close to the experimental values. Therefore, for the set of systems studied in this work, the results of the highly accurate but computationally expensive HSE06 calculations can be accurately estimated by applying this correction factor to the LDA values, as shown in Fig. 2 (see Table S1 in Supplemental Material [35] for the structures used to obtain the LDA-to-HSE06 correlation). In addition to the 40-atom supercells, we perform calculations using 80-atom supercells (see Fig. S1 in Supplemental Material [35]) for the 75BTO-25NTM $(100)_A$ arrangement to examine the effect of the cell size used in our density-functional-theory (DFT) calculations on the energies and E_g values of the solid solutions. We find that the 40-atom 75BTO-25NTM $(100)_A$-arrangement supercell is less than 0.2 meV/atom higher in total energy relative to the average energy of the 80-atom supercells (see Fig. S2 in Supplemental Material [35]). Similarly, its E_g is higher than that of the 80-atom supercells by less than 0.1 eV. These small differences indicate that the effect of the increased cell size is quite weak and the 40-atom supercells discussed in this work are a good representation of the BTO-NTM system. In an experimental realization of the system, one can expect to obtain the averaged values of the different arrangements discussed here.

III. FORMATION OF BTO-NTM AND BTO-NTW

To examine whether the BTO-NTM and BTO-NTW solid solutions are thermodynamically feasible, we compare their formation energies with the energies of a variety of combinations of competing ternary-oxide product compounds. We assume a solid-state preparation route with a reaction conducted between the BaO, Na$_2$O, TiO$_2$, and MoO$_3$ or WO$_3$ binary oxides to form the BTO-NTM

FIG. 1. BTO-NTM supercells studied, showing the different cation arrangements.

TABLE I. The compositions studied and their arrangements and initial displacements.

	75BTO-25NTM	50BTO-50NTW	75BTO-25NTW	50BTO-50NTW
Arrangement	$(100)_A$	$(100)_A(100)_B$	$(100)_A$	$(100)_A(100)_B$
	$(110)_A$	$(100)_A(110)_B$	$(110)_A$	$(100)_A(110)_B$
	$(111)_A$	$(111)_A(110)_B$	$(111)_A$	$(111)_A(110)_B$
		$(111)_A(111)_B$		$(111)_A(111)_B$
Initial displacement			$x, x\text{-}y, x\text{-}y\text{-}z, z$	

or BTO-NTW solid solutions, respectively. The initial stoichiometric coefficients of the binary-oxide reactants in such a reaction are different for each composition [25NTM (25NTW) or 50NTM (50NTW)] and are given in Table II alongside their formation energy with respect to the constituent atoms (E_F) and the formation energy of the BTO-NTM and BTO-NTW systems (considering the arrangements with the lowest energy for each composition) relative to binary oxides (ΔE_F).

Naturally, a reaction of these binary oxides can yield not only BTO-NTM or BTO-NTW but also other competing ternary oxides (e.g., Na_2MoO_4, $BaWO_4$, and pure $BaTiO_3$) with different stoichiometric ratios. Therefore, to test the thermodynamic feasibility of BTO-NTM and BTO-NTW, their ΔE_F value are compared with the ΔE_F values of the competing ternary compounds (both energies with respect to binary oxides). For comparison, ternary compounds made of the combinations of the constituent elements are chosen and are then sorted according to their stability on the basis of their energy above hull as reported by the Materials Project [36]. The competing ternary oxides and their energies of formation (from the constituent elements) are given in Table S2 in Supplemental Material [35].
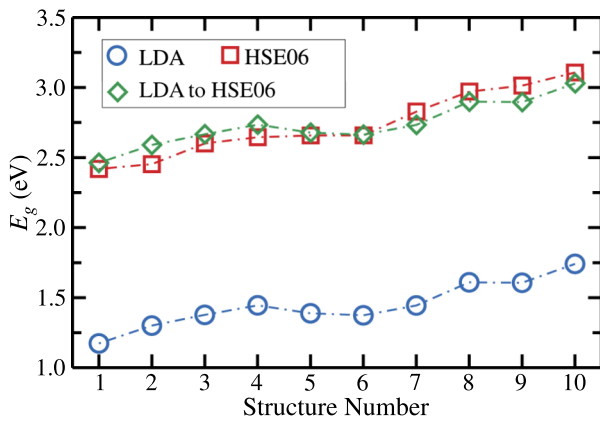
ΔE_F of several products obtained from a reaction with multiple reactants can be calculated with the equation

$$\Delta E_F = \sum_{i=1}^{N_p} x_i E_i - \sum_{j=1}^{N_r} y_j E_j, \qquad (1)$$

where N_p is the number of products, N_r is the number of reactants, E_i and E_j are the formation energy (E_F) of product i and reactant j, respectively, and x and y are the stoichiometric coefficient of the product and reactant, respectively. E_F is the energy of formation from the constituent elements and ΔE_F is the energy of formation from the binary oxides. For the reaction that produces BTO-NTM or BTO-NTW from the above-mentioned binary oxides, Eq. (1) can be redefined as

$$\Delta E_F = \sum_{i=1}^{N_p} x_i E_i - \sum_{j=1}^{4} y_j E_j. \qquad (2)$$

The $\sum_{j=1}^{4} y_j E_j$ term is defined according to the stoichiometric coefficients (Table II) for each of the four BTO-NTM and BTO-NTW compositions studied. For example, for 75BTO-25NTM this term is given by

$$\sum_{j=1}^{4} y_j E_j = E_{Na_2O} + 6E_{BaO} + 7E_{TiO_2} + E_{MoO_3}.$$

The final ΔE_F of the products in this reaction is given by

$$\Delta E_F = \sum_{x=1}^{a} x_i E_i - (E_{Na_2O} + 6E_{BaO} + 7E_{TiO_2} + E_{MoO_3}). \qquad (3)$$

Many possible combinations of products with different ratios can be obtained in the reaction and each combination will yield different ΔE_F values. Our goal is to compare the calculated ΔE_F of BTO-NTM and BTO-NTW systems from binary oxides with the thermodynamically favorable combination of products yielding the lowest ΔE_F.

To determine the favorable products, the ΔE_F values of all possible product combinations in all possible ratios must be compared. Considering the number of possible

FIG. 2. Comparison of LDA, HSE06, and LDA-HSE06 corrected E_g. The LDA-to-HSE06 correction was achieved by our adding the average energy difference between the calculated HSE06 and LDA E_g values (1.29 eV) to the LDA E_g value. See Table S1 in Supplemental Material [35] for the structures used to obtain the correction.

TABLE II. Formation-energy comparison of BTO-NTM and BTO-NTW and the thermodynamically favorable products. For the binary-oxide reagents, the formation energy is given relative to the constituent elements (E_F) and each ratio is the stoichiometric ratio necessary to form the corresponding BTO-NTM or BTO-NTW compound. For the minima, the formation energy is given relative to the binary-oxide reagents.

Binary oxides	E_F	Product	ΔE_F
$Na_2O + 6BaO + 7TiO_2 + MoO_3$	-0.302	$6BaTiO_3 + Na_2MoO_4 + TiO_2$	-0.317
		75BTO-25NTM	-0.302
$2Na_2O + 4BaO + 6TiO_2 + 2MoO_3$	-0.283	$4BaTiO_3 + 2Na_2MoO_4 + 2TiO_2$	-0.303
		50BTO-50NTM	-0.283
$Na_2O + 6BaO + 7TiO_2 + WO_3$	-0.302	$6BaTiO_3 + Na_2WO_4 + TiO_2$	-0.308
		75BTO-25NTW	-0.304
$2Na_2O + 4BaO + 6TiO_2 + 2WO_3$	-0.283	50BTO-50NTW	-0.286

ternary competing products, this is a challenging task. Therefore, we use a basin-hopping global-optimization algorithm [37] to find the stoichiometric coefficients in Eq. (1) that preserve the balance between the right and left sides of the reaction and obtain the minimum value of ΔE_F relative to the reactant binary oxides. The comparison is done for the lowest-energy structure for each of the four BTO-NTM and BTO-NTW compounds. We minimize $\sum_{i=1}^{a} x_i E_i$ while maintaining the stoichimetric ratios of the products (x) balanced to match the stoichiometry of the reactant oxides (y). We allow oxygen addition to the products from O_2 gas as an additional unlimited reagent (in addition to the oxygen sourced from the binary oxides). The O_2 gas is considered to have the enthalpy of an diatomic ideal gas at $1000\,°C$ (unlike the rest of the compounds, for which we use the DFT internal energy). This is equivalent to performing the reaction in an air atmosphere, which allows the addition of O_2 to the solid and conversely the escape of O_2 from the solid state into the atmosphere. Furthermore, the binary oxides are also used as possible products to allow the possibility of partial reaction.

Multiple runs of the basin-hopping-algorithm minimization yield many exothermic reactions with different combinations of products that are formation-energy minima on the overall formation-energy landscape. To evaluate the feasibility of the formation of the target BTO-NTM and BTO-NTW solid solutions, we compare the global minimum (its product ratio and ΔE_F), which represents the thermodynamically-most-favorable outcome of the reaction of binary oxides reaction, and ΔE_F of the reaction yielding BTO-NTM and BTO-NTW systems only. In Fig. 3, we present the ΔE_F values for the formation-energy landscape minima found by the basin-hopping algorithm as a function of the BTO-NTM or BTO-NTW content among the reaction products. Table II compares the compositions and ΔE_F of the global minimum of the reaction with the local minimum that corresponds to the formation of 100% BTO-NTM or BTO-NTW. As can be seen in Table II and Fig. 3, the largest ΔE_F difference between the global minimum and the BTO-NTM and BTO-NTW systems is

approximately 0.02 eV/atom for 50BTO-50NTM, while production of 50BTO-50NTW is found to be the global minimum. For reaction involving Mo, the global minimum comprises a combination of $BaTiO_3$, Na_2MoO_4, and TiO_2. For the reaction involving W, the global minimum comprises a combination of $BaTiO_3$, Na_2WO_4, and TiO_2 for the 75BTO-25NTW stoichiometry of reactants and 50BTO-50NTW for the 50BTO-50NTW stoichiometry of reactants. While the formation energy of the target BTO-NTM and BTO-NTW compositions is not always the global minimum, it is only slightly higher even for the Mo-based compositions. Therefore, it may be possible to synthesize these compounds by manipulating the kinetics to favor the perovskite structure, for example, by using $BaTiO_3$ as the starting reagent or by growing these materials as thin films on a perovskite substrate as was previously done for $PbVO_3$, $BiFe_{1/2}Cr_{1/2}O_3$, and $BiZn_{1/2}Ti_{1/2}O_6$ [38–40], which cannot be synthesized by standard solid-state synthesis routes.
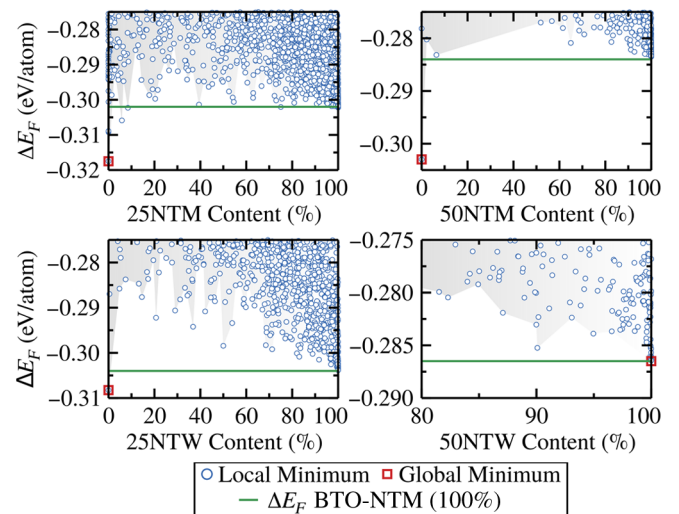

FIG. 3. Local minima as a function of BTO-NTM or BTO-NTW content, shown with respect to ΔE_F from binary oxides required to yield 100% BTO-NTM or BTO-NTW.

IV. PROPERTIES OF BTO-NTM AND BTO-NTW

We begin our property analysis for BTO-NTM and BTO-NTW. Examination of the P values obtained shows many cases of unequal nonzero polarization components, presenting as intermediate phases between the FE T, O, and R phases. Therefore, we use the notation introduced by Vanderbilt and Cohen [41] to describe the structures obtained, with M_A, M_B, and M_C denoting the phases between the T and R phases, between the R and O phases, and between the T and O phases, respectively.

The results obtained for P_x, P_y, P_z, total P (P_{tot}), LDA and HSE06 E_g values, and energies relative to the lowest-energy structure for a given composition are shown in Table III for BTO-NTM and in Table IV for BTO-NTW. The results for parent BaTiO$_3$ as well as additional information regarding the conduction-band minimum (CBM), valence-band maximum (VBM), and unit-cell volume of the compositions studied can be found in Tables S3–S5 in Supplemental Material [35].

A. Effects of compositional variation

Examination of the E_g and P values obtained for the relaxed BTO-NTM and BTO-NTW structures shows that NTM or NTW substitution induces significant changes in E_g and P_{tot}, as can be seen in Fig. 4. As expected, introduction of Mo into the BaTiO$_3$ structure lowers E_g, with an average E_g decrease of 0.6 eV for 75BTO-25NTM and 0.87 eV for 50BTO-50NTM relative to BaTiO$_3$. Similarly, introduction of W into BaTiO$_3$ decreases E_g by 0.32 eV for 75BTO-25NTW and by 0.68 eV for 50BTO-50NTW on average relative to BaTiO$_3$. Introduction of Mo or W largely maintains the polarization of of the parent BaTiO$_3$. In particular, E_g obtained for 75BTO-25NTM (approximately 2.8 eV) is ideal for transparent photovoltaics, while absorption in the near-UV range and in the visible

TABLE III. A-site and B-site arrangements, initial displacement, phase obtained (determined by P), HSE06 E_g (obtained by addition of the LDA-to-HSE06 correction) and LDA E_g (in parentheses), ΔE (energy relative to the lowest-energy structure with the same composition), calculated P magnitudes, deviation angle α, direct (D) or indirect (I) band gap, and tolerance factor (t) for the different BTO-NTM compositions.

A-site arrangement	B-site arrangement	Displacement	Phase	E_g (eV)	D or I	ΔE (meV/atom)	P_{tot} (P_x, P_y, P_z) (C/m^2)	α (deg)
75BTO-25NTM ($t = 1.047$)								
$(100)_A$	None	x	M_A	2.67 (1.38)	I	0.00	0.35 (0.29, 0.13, 0.13)	4.89
		x-y	O	2.74 (1.45)	D	0.09	0.35 (0.27, 0.23, 0.03)	4.87
		x-y-z	M_A	2.76 (1.47)	I	0.07	0.35 (0.24, 0.18, 0.18)	5.83
		z	T	2.62 (1.33)	D	0.45	0.33 (0.00, 0.07, 0.32)	2.87
$(110)_A$	None	x	T	2.47 (1.18)	I	1.35	0.36 (0.36, 0.00, 0.00)	0.00
		x-y	O	2.70 (1.41)	D	1.12	0.36 (0.26, 0.25, 0.04)	5.23
		x-y-z	M_A	2.71 (1.42)	D	1.07	0.35 (0.24, 0.18, 0.18)	5.84
		z	M_B	2.75 (1.46)	D	1.12	0.36 (0.17, 0.21, 0.24)	6.36
$(111)_A$	None	x	M_A	2.60 (1.31)	D	3.70	0.35 (0.32, 0.09, 0.09)	3.44
		x-y	M_A	2.73 (1.44)	D	3.51	0.37 (0.18, 0.18, 0.26)	5.98
		x-y-z	R	2.72 (1.43)	D	3.81	0.33 (0.19, 0.19, 0.19)	6.05
		z	M_A	2.60 (1.31)	D	3.70	0.35 (0.09, 0.09, 0.32)	3.44
50BTO-50NTM ($t = 1.028$)								
$(100)_A$	$(100)_B$	x	T	2.64 (1.35)	D	7.14	0.40 (0.40, 0.00, 0.00)	0.00
		x-y	M_C	2.58 (1.29)	D	7.27	0.40 (0.36, 0.17, 0.00)	3.00
		x-y-z	M_A	2.59 (1.30)	D	7.30	0.40 (0.35, 0.13, 0.13)	4.03
		z	T	1.82 (0.53)	D	10.36	0.30 (0.00, 0.00, 0.30)	3.14
$(100)_A$	$(110)_B$	x	T	1.66 (0.37)	I	1.32	0.36 (0.36, 0.00, 0.00)	0.00
		x-y	M_C	2.31 (1.02)	I	0.61	0.39 (0.17, 0.35, 0.00)	3.62
		x-y-z	O	2.42 (1.13)	I	0.00	0.37 (0.05, 0.26, 0.26)	7.48
		z	M_C	2.52 (1.23)	I	0.01	0.39 (0.11, 0.00, 0.38)	3.64
$(111)_A$	$(110)_B$	x	T	1.62 (0.33)	I	5.40	0.36 (0.36, 0.00, 0.00)	0.00
		x-y	M_C	2.32 (1.03)	D	4.25	0.41 (0.22, 0.34, 0.04)	4.98
		x-y-z	M_B	2.32 (1.03)	D	4.36	0.40 (0.16, 0.26, 0.26)	7.08
		z	T	2.52 (1.23)	I	4.39	0.41 (0.00, 0.00, 0.41)	0.00
$(111)_A$	$(111)_B$	x	T	2.66 (1.37)	D	3.66	0.39 (0.39, 0.00, 0.00)	0.00
		x-y	O	2.86 (1.57)	D	3.32	0.39 (0.27, 0.27, 0.00)	6.36
		x-y-z	R	2.96 (1.67)	D	2.95	0.38 (0.22, 0.22, 0.22)	7.02
		z	T	2.66 (1.37)	D	3.66	0.39 (0.00, 0.00, 0.39)	0.00

TABLE IV. *A*-site and *B*-site arrangements, initial displacement, phase obtained (determined by P), HSE06 E_g (obtained by addition of the LDA-to-HSE06 correction) and LDA E_g (in parentheses), ΔE (energy relative to the lowest-energy structure with the same composition), calculated P magnitudes, deviation angle α, direct (D) or indirect (I) band gap, and tolerance factor (t) for the different BTO-NTW compositions.

A-site arrangement	*B*-site arrangement	Displacement	Phase	E_g (eV)	D or I	ΔE (meV/atom)	P_{tot} (P_x, P_y, P_z) (C/m^2)	α (deg)
75BTO-25NTW ($t = 1.046$)								
$(100)_A$	None	x	R	3.03 (1.74)	D	0.04	0.32 (0.22, 0.17, 0.17)	5.63
		x-y	M_B	3.04 (1.75)	D	0.00	0.33 (0.23, 0.17, 0.16)	5.53
		x-y-z	R	3.04 (1.75)	D	0.05	0.33 (0.20, 0.18, 0.18)	5.57
		z	O	2.94 (1.65)	D	0.43	0.32 (0.00, 0.22, 0.23)	3.95
$(110)_A$	None	x	T	2.74 (1.45)	D	1.97	0.29 (0.29, 0.00, 0.00)	0.00
		x-y	O	2.95 (1.66)	D	1.35	0.31 (0.20, 0.23, 0.00)	4.63
		x-y-z	R	2.99 (1.70)	D	1.20	0.31 (0.18, 0.18, 0.18)	5.61
		z	O	2.96 (1.67)	D	1.32	0.31 (0.20, 0.02, 0.24)	4.77
$(111)_A$	None	x	T	2.95 (1.66)	D	3.40	0.24 (0.23, 0.05, 0.05)	5.31
		x-y	O	2.90 (1.61)	D	3.87	0.31 (0.22, 0.22, 0.02)	4.68
		x-y-z	R	2.97 (1.68)	D	3.47	0.30 (0.17, 0.17, 0.17)	5.68
		z	T	2.95 (1.66)	D	3.40	0.24 (0.05, 0.05, 0.23)	5.31
50BTO-50NTW ($t = 1.027$)								
$(100)_A$	$(100)_B$	x	T	2.79 (1.50)	I	10.18	0.33 (0.33, 0.00, 0.00)	0.00
		x-y	M_C	2.68 (1.39)	D	10.10	0.34 (0.29, 0.17, 0.00)	2.91
		x-y-z	M_A	2.68 (1.39)	D	10.01	0.33 (0.27, 0.14, 0.14)	4.16
		z	T	2.21 (0.92)	D	11.24	0.27 (0.00, 0.00, 0.27)	3.30
$(100)_A$	$(110)_B$	x	T	2.09 (0.80)	D	1.11	0.28 (0.28, 0.00, 0.00)	0.00
		x-y	M_C	2.43 (1.14)	D	1.02	0.33 (0.16, 0.28, 0.00)	3.49
		x-y-z	M_B	2.48 (1.19)	D	1.04	0.33 (0.11, 0.22, 0.22)	6.24
		z	M_C	2.56 (1.27)	D	0.00	0.33 (0.17, 0.00, 0.28)	4.03
$(111)_A$	$(110)_B$	x	T	2.03 (0.74)	I	4.53	0.31 (0.31, 0.00, 0.00)	0.00
		x-y	M_B	2.41 (1.12)	I	4.14	0.34 (0.21, 0.26, 0.07)	5.19
		x-y-z	R	2.41 (1.12)	D	4.13	0.35 (0.19, 0.21, 0.21)	6.60
		z	T	2.61 (1.32)	I	4.95	0.35 (0.00, 0.00, 0.35)	0.00
$(111)_A$	$(111)_B$	x	T	2.90 (1.61)	D	4.73	0.33 (0.33, 0.00, 0.00)	0.00
		x-y	O	3.11 (1.82)	D	3.96	0.34 (0.24, 0.24, 0.00)	5.32
		x-y-z	R	3.24 (1.95)	D	3.36	0.34 (0.20, 0.20, 0.20)	6.56
		z	T	2.90 (1.61)	D	4.73	0.33 (0.00, 0.00, 0.33)	0.00

range is obtained for 50BTO-50NTM and 50BTO-50NTW depending on the arrangement of the *B*-cation substituent atoms.

Both the decrease in E_g and the small changes in P can be easily understood. The substitution of the more-electronegative Mo for Ti leads to a decrease in the band gap. For P, the introduction of the more-anomalous Z^* Born effective charge of Mo leads to a greater contribution of the *B* site to P. Similar anomalous Z^* was previously reported for WO_3 [42] (see Table S6 in Supplemental Material [35] for comparison of Z^* between MoO_3, WO_3, and $BaTiO_3$ perovskites). Additionally, the replacement of the larger Ba by the smaller Na enhances the displacement at the *A* site, which also is favorable for larger P. This is similar to the larger displacement of the Ca cations (which have cation radius similar to that of Na cations) on substitution into $BaTiO_3$ [18]. On the other hand, the substitution of the smaller Na *A*-site atoms decreases the volume of the

system, favoring smaller P magnitudes [26]. It appears that these two effects largely cancel each other.

Examination of energies for each composition (Tables III and IV) shows that the M_A and M_B phases are the stablest for 75BTO-25NTM and 75BTO-25NTW, respectively, whereas 50BTO-50NTM and 50BTO-50NTW prefer the O and M_C phases, respectively. Examination of the results for BTO-NTW shows the same E_g and P trends as observed for BTO-NTM, but with blueshifts of the E_g values of approximately 0.24 eV and decrease of the P values by approximately 0.05 C/m^2. Both the higher E_g values and the smaller P values are due to the weaker electronegativity of W compared with Mo. This leads to a more-ionic bond and smaller Jahn-Teller-distortion driving force such that a larger band gap and smaller displacement, Z^*, and P are obtained for BTO-NTW. We find that the PES with respect to the rotation of the polarization vector is more isotropic for 75BTO-25NTM
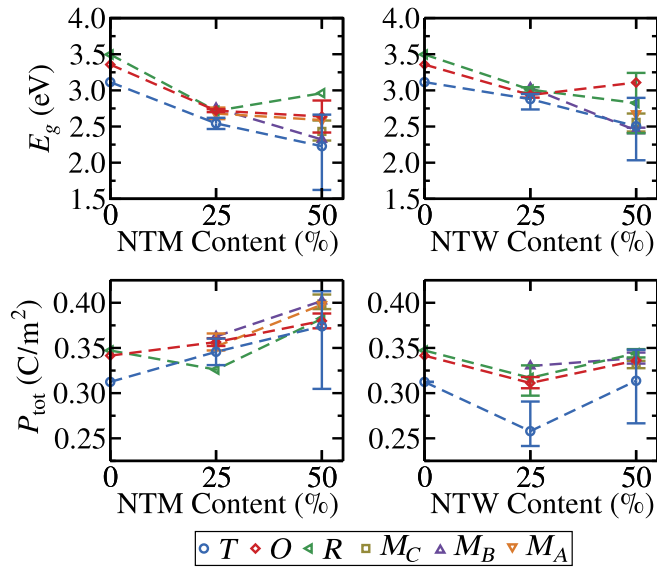
FIG. 4.   Effect of NTM or NTW substitution on E_g (HSE06) and P for different phases obtained. The error bars indicate the variations of E_g or P between different structures in the same phase and with the same composition.

and 75BTO-25NTW than for BaTiO$_3$, 50BTO-50NTM, or 50BTO-50NTW, with particularly small polarization-rotation energies obtained for 75BTO-25NTW. For example, the R, O, and T phases have the same energy for the $(111)_A$ arrangement of 75BTO-25NTW, and the M_A phase is the stablest for all the 75BTO-25NTM $(100)_A$, $(110)_A$, and $(111)_A$ arrangements. Therefore, we perform piezoelectric coefficient calculations for each composition for the lowest-energy phase other than the T phase. Despite the low energy difference between the different polarization orientations, the increase in the piezoelectric coefficients relative to BaTiO$_3$ is rather modest, with d_{33} of 124.1 and 71.7 pC/N for 50BTO-50NTW and BaTiO$_3$, respectively (see Table S7 in Supplemental Material [35] for more piezoelectric coefficients).

B. Effects of cation arrangement and polarization direction

A more-in-depth analysis of the DFT results reveals the effects of cation arrangement and polarization orientation on the properties of BTO-NTM and BTO-NTW solid solutions. Specifically, for 50BTO-50NTM and 50BTO-50NTW, while for the $(111)_A(111)_B$ arrangements of the polarization orientation along all of the Cartesian axes are equivalent, for the rest of the arrangements the displacements are inequivalent with respect to the Na and Ba stacking direction or the B-site orientation. The different polarization orientations relative to the cation stacking may change the properties of the material. Thus, the 50BTO-50NTM and 50BTO-50NTW structures with the

$(100)_A$ A-site arrangement that are x displaced are displaced perpendicular to the Na and Ba stacking and those that are z displaced are displaced parallel to the Na and Ba stacking. In addition, x-axis displacement in the $(110)_B$ B-site arrangements of 50BTO-50NTM and 50BTO-50NTW results in displacement perpendicular to the Mo- or W-containing B-site plane, which has a high content of over-bonded oxygens (due to the higher valence of the Mo and W cations relative to Ti) [43]. This is also present in the $(100)_A(100)_B$ arrangement when displaced along the z axis. However, it is important to mention that the displacements specified here are the initial displacements only, which do not necessarily correspond to the final polarization-vector direction obtained after the relaxation. All structures with displacement perpendicular to the plane with a high content of overbonded oxygens have minima in the T phase.

1. 75BTO-25NTM and 75BTO-25NTW

Examination of the relative energies of the different cation arrangements shows that the $(100)_A$ arrangement is the stablest for 75BTO-25NTM and 75BTO-25NTW [Fig. 5(a)]. Comparison of the 75BTO-25NTM and 75BTO-25NTW structures shows that the cation arrangement has a weak effect on E_g, with variation of at most approximately 0.3 eV between the different cation arrangements, as can be seen in Fig. 5(b). Variation of polarization orientation has a similarly small effect on
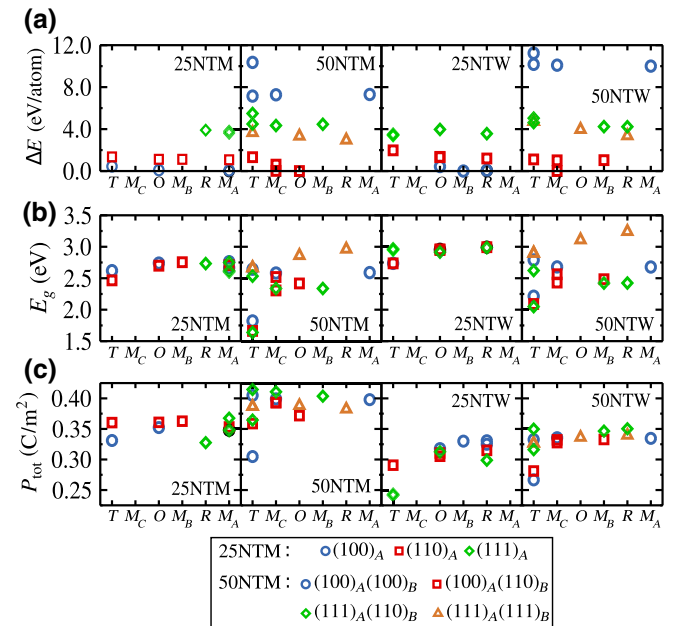

FIG. 5.   Phase and arrangement effect on (a) relative energy (compared with the lowest-energy structure for each composition), (b) P_{tot}, and (c) E_g for the different BTO-NTM and BTO-NTW compositions.
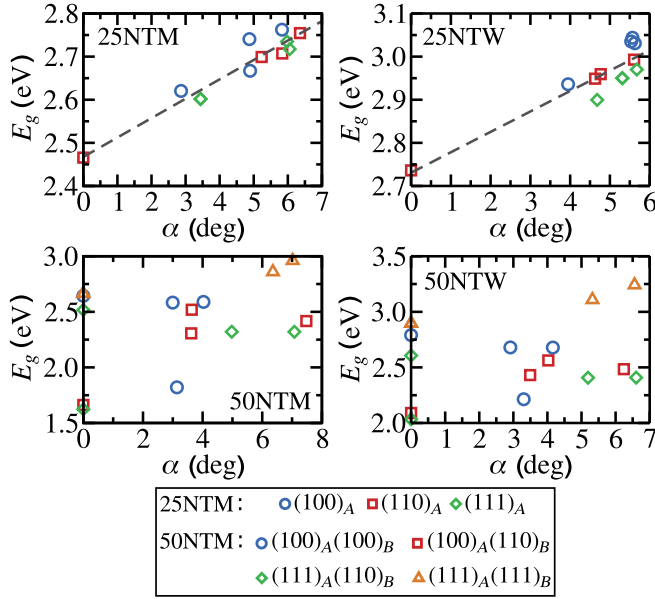
FIG. 6. Dependence of E_g on α, the minimal deviation from 180° in the O-B-O angle, averaged over all the B sites for each structure. The dashed line shows the linear regression of the calculated α values for the composition.

E_g, with several structures of a given arrangement with different polarization orientation showing similar E_g values. The P magnitudes also exhibit low sensitivity to the variation both in the cation substituent arrangement and polarization orientation, with variations of P_{tot} of at most approximately 0.05 C/m^2 observed, as can be seen in Fig. 5(c). Previous work demonstrated the importance of the O-B-O angle for E_g in ABO_3 materials [13,25]. The metal-oxygen chain with the lowest angle gives the CBM, which in turns controls E_g, and each B-site cation in the system participates in three O-B-O angles. For each B site, we take the O-B-O angle with the smallest deviation from 180°, calculate the average of these angles (α), and plot E_g as a function of α for different structures for the different compositions in Fig. 6. Examination of Fig. 6 shows that for 75BTO-25NTM and 75BTO-25NTW, a clearly linear relationship exists between E_g and α.

2. 50BTO-50NTM and 50BTO-50NTW

For 50BTO-50NTM and 50BTO-50NTW, the $(100)_A$ $(110)_B$ arrangement is the stablest, as shown in Fig. 5(a). The variation in E_g between the different cation arrangements and polarization orientations can be large, with a particularly small E_g (1.6–1.8 eV) obtained for the z-displaced $(100)_A(100)_B$, x-displaced $(100)_A(110)_B$, and x-displaced $(111)_A(110)_B$ arrangements of 50BTO-50NTM. The same trend is observed for the same arrangements and displacements of 50BTO-50NTW. The common feature among these three low-E_g structures is that

their polarization is perpendicular to the above-mentioned plane with high overbonded-oxygen content (giving the T phase). Variations in the P magnitude are relatively small for 50BTO-50NTM and 50BTO-50NTW, and the energy differences between the different polarization orientations are larger than those for 75BTO-25NTM and 75BTO-25NTW. The low band gap of the 50BTO-50NTM structures shows that visible-light absorption can be induced by Mo doping. In addition, the low relative energy difference (1.321 meV/atom) between the energetically favorable 50BTO-50NTM O-phase $(100)_A(110)_B$ (E_g of 2.42 eV) and the visible-light absorber with the lowest-energy T-phase $(100)_A(110)_B$ (E_g of 1.66 eV) suggests that the mentioned induction of visible-light absorption via Mo substitution is feasible. The large relative energy (compared for the composition) difference between the energetically favorable 50BTO-50NTM [O-phase $(100)_A(110)_B$] and the low-band-gap T-phase $(100)_A(100)_B$ (which gives rise to the Mo-O-Mo chain) arrangements in the composition suggests that the low-band-gap Mo-O-Mo configuration is unlikely to be common. Therefore, on the basis of the properties of the lowest-energy structure, 50BTO-50NTM is likely to exhibit visible-light-absorbing properties in its T phase, or E_g of approximately 2.6 eV on realization in other phases.

The E_g trends of 50BTO-50NTM and 50BTO-50NTW cannot be explained with use of α, as they deviate from the linear trend that was observed for 75BTO-25NTM and 75BTO-25NTW. This suggests that while the effects of deviation from the 180° O-B-O angle are also present in these compositions, they are dominated by the effects of the interplay of the B-cation ordering and polarization orientation, which in some cases give rise to a much lower E_g, as discussed below. The BTO-NTW results show similar trends to the BTO-NTM results, but with all E_g values shifted up due to the weaker electronegativity of W^{6+}.

3. B-cation ordering and polarization orientation effects on the band gap

We now discuss the structural features that give rise to the observed E_g variation for a given BTO-NTM or BTO-NTW composition. Considering the low band gaps found for several 50BTO-50NTM and 50BTO-50NTW structures, it is clear that E_g is governed by additional factors besides α. To elucidate the effects controlling E_g, we perform calculations for additional structures with arrangements of $(100)_A(111)_B$, $(111)_A(100)_B$, and $(010)_A(100)_B$, without imposing initial displacements. These arrangements are illustrated in Fig. 7. In addition, we perform additional calculations for the already-mentioned $(100)_A(100)_B$, $(100)_A(110)_B$, $(111)_A(110)_B$, and $(111)_A(100)_B$ arrangements of 50BTO-50NTM without imposing initial displacements. The results for all the initially nondisplaced arrangements are given in Table V.
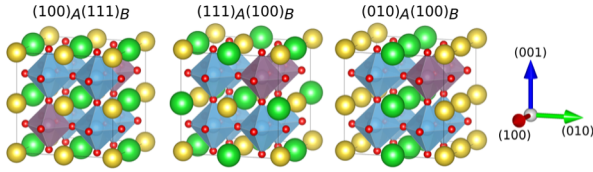
FIG. 7. Additional 50BTO-50NTM cation arrangements studied.

Examination of Table V shows that although no initial displacements were imposed, most structures relax to a T-phase minimum, while the $(100)_A(100)_B$ and $(111)_A(100)_B$ structures did relax to a minimum in the C phase (nondisplaced structures). Comparison of these nondisplaced structures shows that the A-site influence on E_g is rather weak, with variation of 0.05 eV between these two structures (which exhibit the same B-site arrangement and different A-site arrangement). For the T-phase structures, such weak influence of the A-site arrangement is also found for the structures that have the same B-site arrangement and different A-site arrangements. This is consistent with the results obtained for the initially displaced 50BTO-50NTM and 50BTO-50NTW $(100)_A(110)_B$ and $(111)_A(110)_B$ arrangements (Tables III and IV) that show a variation of approximately 0.05 eV between the structures displaced in the same direction (for example, the x-displaced 50BTO-50NTM $(100)_A(110)_B$ and $(111)_A(110)_B$ arrangements have E_g of 1.66 and 1.62 eV, respectively).

The B-site arrangement itself has a strong effect on E_g. Comparing structures with the same polarization direction, the same A-site arrangement, and the different B-site arrangements, we find E_g varies strongly for the T phase. This effect is slightly weaker for the phases with multiple polarization directions (R, O, and monoclinic phases). This is connected to the effect of the polarization direction on E_g. For a given arrangement, the phases with multiple polarization directions (R, O, and monoclinic phases) will exhibit higher E_g than the T phase. This effect of the T phase having the lowest E_g is amplified in the structures that have polarization in the direction

perpendicular to Mo- or W-containing B-site planes, for which all O atoms are overbonded [43]; for these structures, E_g decreases by approximately 1 eV relative to the structure polarized parallel to the plane, as mentioned above. This effect emphasizes the importance of not only the B-site arrangement but also the B-site displacement orientation, which together control the band gap. Figure 8 shows the band structure and density of states for the $(100)_A(110)_B$ and $(100)_A(100)_B$ structures of 50BTO-50NTM in their energetically favorable structure (x-y-z displaced and x displaced, respectively), the lowest-E_g structures (x displaced and z displaced, respectively), and the initially nondisplaced structures. Examination of the band-structure plots in Fig. 8 shows that the effect on E_g of the orientation of the polarization relative to the Mo- or W-containing B-site planes influences the CBM mostly, with the conduction band becoming wider for the lower-band-gap T-phase structures. Examination of the density of states shows that, as expected, the CBM comprises the Mo and Ti d states with a small amount of the O $2p$ state. Therefore, our calculations reveal the existence of coupling between the CBM position and the displacement direction of the B-site cations in this system. The effect of polarization rotation may be present in other systems, but most likely is amplified (approximately 1 eV) in this system by Mo (compared with approximately 0.6 eV for W) and will be weaker in other perovskites with smaller valence of the B-site cation [13].

To summarize, E_g is governed by the following factors:

(a) As mentioned in Sec. IV, replacement of the less-electronegative Ti^{+4} cation with the more-electronegative Mo^{+6} cation decreases E_g.

(b) The deviation angle α influences the overlap between B d and O $2p$ orbitals and increases E_g with larger deviation from $180°$ (Fig. 6). This effect governs the E_g trends of 75BTO-25NTM and 75BTO-25NTW but does not explain the trends observed for 50BTO-50NTM and 50BTO-50NTW.

(c) For the B-site arrangements containing a B-site plane where all O atoms are overbonded, polarization

TABLE V. Cation (A and B) arrangement, phase obtained after relaxation of ionic coordinates , LDA VBM and CBM, HSE06 E_g, and P magnitudes of the initially nondisplaced 50BTO-50NTM structures used for comparison of the influence of the arrangement.

| A-site arrangement	B-site arrangement	Phase	E_g (eV)	VBM (eV)	CBM (eV)	P_{tot} (P_x, P_y, P_z) (C/m^2)	Illustration
$(010)_A$	$(100)_B$	T	1.72	9.33	9.76	0.27 (0.00, 0.27, 0.00)	Figure 7
$(100)_A$	$(100)_B$	C	1.87	9.31	9.88	0.00 (0.00, 0.00, 0.00)	Figure 1
$(111)_A$	$(100)_B$	C	1.72	9.36	9.79	0.00 (0.00, 0.00, 0.00)	Figure 7
$(100)_A$	$(110)_B$	T	1.67	9.34	9.71	0.30 (0.30, 0.00, 0.00)	Figure 1
$(111)_A$	$(110)_B$	T	2.49	9.14	10.35	0.39 (0.00, 0.00, 0.39)	Figure 1
$(100)_A$	$(111)_B$	T	2.67	9.02	10.4	0.33 (0.33, 0.00, 0.00)	Figure 7
$(111)_A$	$(111)_B$	T	2.67	8.97	10.35	0.37 (0.37, 0.00, 0.00)	Figure 1
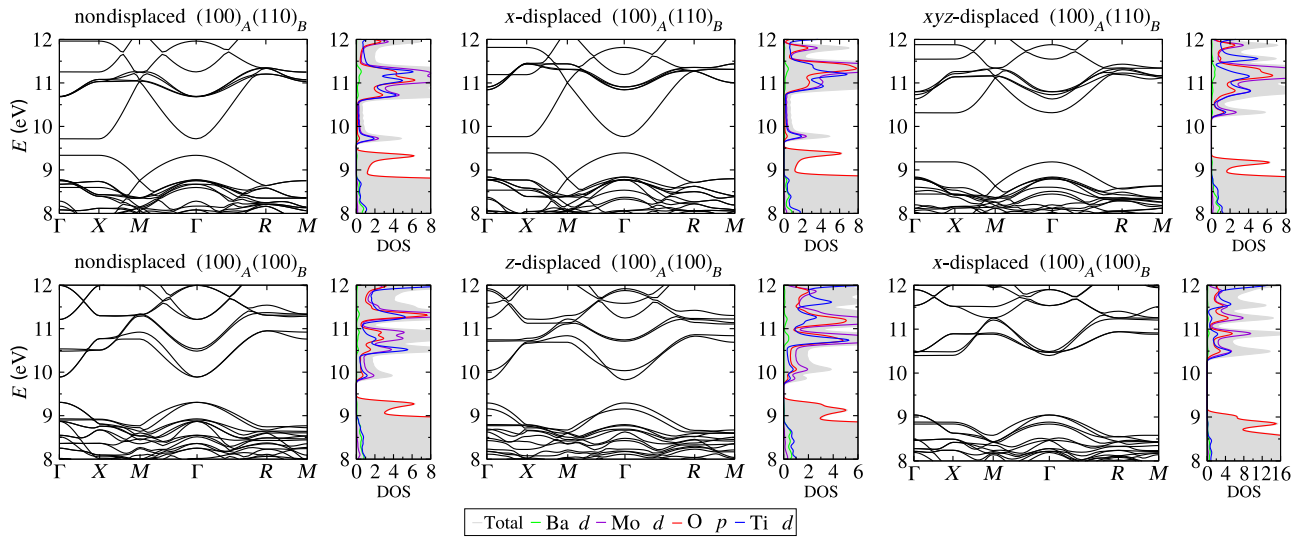
FIG. 8.   Band structures, projected density of states (DOS) and total DOS (filled area) for 50BTO-50NTM $(100)_A(110)_B$ (with initial x-y-z and x displacements and no displacement) and $(100)_A(100)_B$ (with initial x and z displacements and no displacement), showing the large variation of E_g with polarization rotation.

perpendicular to this plane gives low E_g values, while polarization parallel to this plane gives high E_g values. The origin of this effect is currently unclear and will be investigated in future work.

V. CONCLUSION

We study the effect of joint Na and Mo (W) substitution in BaTiO$_3$ on the electronic structure and P. It is found that the E_g values obtained with use of the highly accurate and computationally expensive HSE06 hybrid functional can be predicted by a rigid upward shift (1.29 eV) of the LDA-obtained values for this material. 75BTO-25NTM shows a significant E_g lowering of 0.6 eV relative to the parent BaTiO$_3$, with E_g of 2.8 eV. The E_g value obtained is ideal for a fully transparent PV, and since in practice one can expect a combination of the arrangements investigated on synthesis, it is likely that the band gap will be direct. Such a direct bad gap is vital for achieving high efficiency in BPVE-based devices. For 50BTO-50NTM, it is found that E_g has a strong dependence on the arrangement of the Mo atoms and the polarization direction, with E_g ranging from 1.66 to 2.96 eV. By contrast, the arrangement of A-site atoms has little effect on E_g. Substitution of W has similar effects to Mo substitution but with an upshift of E_g due to the lower effective electronegativity of the W^{6+} cation. Taken together, the results of our calculations show that E_g in these solid solutions is controlled by three factors: the intrinsic effective electronegativity of the substituent +6 cation, the distortion of the O-B-O angle α from 180°, and the enhanced mixing of the Mo (W) and O states in the structures polarized perpendicular or parallel to the plane where all O atoms are overbonded. All compositions

display strong polarization that can enable hot-carrier PCE beyond the Shockley-Queiser limit with nanoscale electrodes. Compared with the parent BaTiO$_3$, which has a larger indirect bad gap and lower P, BTO-NTM and BTO-NTW are expected to show stronger BPVE and better PV performance due to their lower E_g, direct character of the band gap, and greater polarization. Additionally, BTO-NTM and BTO-NTW are expected to have a higher Curie temperature and contain only nontoxic and Earth-abundant elements. These properties may enable them to play a key role in the future development of transparent FE-based PV devices.

[1] Jonathan E. Spanier, Vladimir M. Fridkin, Andrew M. Rappe, Andrew R. Akbashev, Alessia Polemi, Yubo Qi, Zongquan Gu, Steve M. Young, Christopher J. Hawley, Dominic Imbrenda, Geoffrey Xiao, Andrew L. Bennett-Jackson, and Craig L. Johnson, Power conversion efficiency exceeding the Shockley-Queisser limit in a ferroelectric insulator, Nat. Photonics **10**, 611 (2016).

[2] Charles Paillard, Xiaofei Bai, Ingrid C. Infante, Maël Guennou, Grégory Geneste, Marin Alexe, Jens Kreisel, and Brahim Dkhil, Photovoltaics with ferroelectrics: Current status and beyond, Adv. Mater. **28**, 5153 (2016).

[3] Keith T. Butler, Jarvist M. Frost, and Aron Walsh, Ferroelectric materials for solar energy conversion: Photoferroics revisited, Energy Environ. Sci. **8**, 838 (2015).

[4] Liang Z. Tan, Fan Zheng, Steve M. Young, Fenggong Wang, Shi Liu, and Andrew M. Rappe, Shift current bulk photovoltaic effect in polar materials-hybrid and oxide perovskites and beyond, npj Comput. Mater. **2,** 16026 (2016).

[5] Zhen Fan, Kuan Sun, and John Wang, Perovskites for photovoltaics: A combined review of organic-inorganic halide perovskites and ferroelectric oxide perovskites, J. Mater. Chem. A **3,** 18809 (2015).

[6] Yang Bai, Pavel Tofel, Jaakko Palosaari, Heli Jantunen, and Jari Juuti, A game changer: A multifunctional perovskite exhibiting giant ferroelectricity and narrow bandgap with potential application in a truly monolithic multienergy harvester or sensor, Adv. Mater. **29,** 1 (2017).

[7] A. Zenkevich, Yu Matveyev, K. Maksimova, R. Gaynutdinov, A. Tolstikhina, and V. Fridkin, Giant bulk photovoltaic effect in thin ferroelectric $BaTiO_3$ films, Phys. Rev. B **90,** 1 (2014).

[8] R. Nechache, C. Harnagea, S. Li, L. Cardenas, W. Huang, J. Chakrabartty, and F. Rosei, Bandgap tuning of multiferroic oxide solar cells, Nat. Photonics **9,** 61 (2014).

[9] Ilya Grinberg, D. Vincent West, Maria Torres, Gaoyang Gou, David M. Stein, Liyan Wu, Guannan Chen, Eric M. Gallo, Andrew R. Akbashev, Peter K. Davies, Jonathan E. Spanier, and Andrew M. Rappe, Perovskite oxides for visible-light-absorbing ferroelectric and photovoltaic materials, Nature **503,** 509 (2013).

[10] Jiangang He, Cesare Franchini, and James M. Rondinelli, Lithium niobate-type oxides as visible light photovoltaic materials, Chem. Mater. **28,** 25 (2016).

[11] Woo Seok Choi, Matthew F. Chisholm, David J. Singh, Taekjib Choi, Gerald E. Jellison, Jr., Ho Nyung Lee, Gerald E. Jellison, and Ho Nyung Lee, Wide bandgap tunability in complex transition metal oxides by site-specific substitution, Nat. Commun. **3,** 689 (2012).

[12] Gaoyang Gou, Nenian Charles, Jing Shi, and James M. Rondinelli, A-site ordered double perovskite $CaMnTi_2O_6$ as a multifunctional piezoelectric and ferroelectric-photovoltaic material, Inorg. Chem. **56,** 11854 (2017).

[13] Fenggong Wang, Ilya Grinberg, and Andrew M. Rappe, Band gap engineering strategy via polarization rotation in perovskite ferroelectrics, Appl. Phys. Lett. **104,** 152903 (2014).

[14] V. I. Belinicher and B. I. Sturman, The photogalvanic effect in media lacking a center of symmetry, Sov. Phys. Usp. **23,** 199 (1980).

[15] S. C. Abrahams, S. K. Kurtz, and P. B. Jamieson, Atomic displacement relationship to curie temperature and spontaneous polarization in displacive ferroelectrics, Phys. Rev. **172,** 551 (1968).

[16] Ilya Grinberg and Andrew M. Rappe, Local structure and macroscopic properties in $PbMg_{1/3}Nb_{2/3}O_3$–$PbTiO_3$ and $PbZn_{1/3}Nb_{2/3}O_3$–$PbTiO_3$ solid solutions, Phys. Rev. B **70,** 220101 (2004).

[17] Ruihao Yuan, Zhen Liu, Prasanna V. Balachandran, Deqing Xue, Yumei Zhou, Xiangdong Ding, Jun Sun, Dezhen Xue, and Turab Lookman, Accelerated discovery of large electrostrains in $BaTiO_3$-Based piezoelectrics using active learning, Adv. Mater. **30,** 1 (2018).

[18] Desheng Fu, Mitsuru Itoh, Shin Ya Koshihara, Taichi Kosugi, and Shinji Tsuneyuki, Anomalous Phase Diagram of Ferroelectric $(Ba, Ca)TiO_3$ Single Crystals with Giant Electromechanical Response, Phys. Rev. Lett. **100,** 227601 (2008).

[19] Atal Bihari Swain, D. Murali, B. R. K. Nanda, and Pattukkannu Murugavel, Large Bulk Photovoltaic Response by Symmetry-Breaking Structural Transformation in Ferroelectric $[Ba(Zr_{0.2}Ti_{0.8}O_3]_{0.5}[(Ba_{0.7}Ca_{0.3})TiO_3]_{0.5}$, Phys. Rev. Appl. **11,** 44007 (2019).

[20] I. C. Amaechi, G. Kolhatkar, A. Hadj Youssef, D. Rawach, S. Sun, and A. Ruediger, B-site modified photoferroic Cr^3+-doped barium titanate nanoparticles: Microwave-assisted hydrothermal synthesis, photocatalytic and electrochemical properties, RSC Adv. **9,** 20806 (2019).

[21] Lakshmi Kola, D. Murali, Subhajit Pal, B. R. K. Nanda, and P. Murugavel, Enhanced bulk photovoltaic response in Sn doped $BaTiO_3$ through composition dependent structural transformation, Appl. Phys. Lett. **114,** 183901 (2019).

[22] Qiwei Lou, Jiangtao Zeng, Zhenyong Man, Liaoying Zheng, Chulhong Park, Abdelhadi Kassiba, Yun Liu, Xiaoming Chen, and Guorong Li, The effect of grain boundary on the visible light absorption of $BaTi_{1-x}[Ni_{1/2}Nb_{1/2}]_xO_{3-\delta}$ ferroelectric ceramics, J. Am. Ceram. Soc. **102,** 7405 (2019).

[23] Pengcheng Xie, Fan Yang, Renjie Li, Changzhi Ai, Chunfu Lin, and Shiwei Lin, Improving hydrogen evolution activity of perovskite $BaTiO_3$ with Mo doping: Experiments and first-principles analysis, Int. J. Hydrogen Energy **44,** 11695 (2019).

[24] Fan Yang, Shiwei Lin, Liang Yang, Jianjun Liao, Yongjun Chen, and Cai Zhuang Wang, First-principles investigation of metal-doped cubic $BaTiO_3$, Mater. Res. Bull. **96,** 372 (2017).

[25] Hank W. Eng, Paris W. Barnes, Benjamin M. Auer, and Patrick M. Woodward, Investigations of the electronic structure of d^0 transition metal oxides belonging to the perovskite family, J. Solid State Chem. **175,** 94 (2003).

[26] Ronald E. Cohen, Origin of ferroelectricity in perovskite oxides, Nature **358,** 136 (1992).

[27] Richard R. Lunt, Theoretical limits for visibly transparent photovoltaics, Appl. Phys. Lett. **101,** 43902 (2012).

[28] Paolo Giannozzi *et al.*, QUANTUM ESPRESSO: A modular and open-source software project for quantum simulations of materials, J. Phys.: Condens. Matter **21,** 395502 (2009).

[29] Kevin F. Garrity, Joseph W. Bennett, Karin M. Rabe, and David Vanderbilt, Pseudopotentials for high-throughput DFT calculations, Comput. Mater. Sci. **81,** 446 (2014).

[30] Robert G. Parr, Shridhar R. Gadre, and Libero J. Bartolotti, Local density functional theory of atoms and molecules, Proc. Natl. Acad. Sci. **76,** 2522 (1979).

[31] J. P. Perdew and Alex Zunger, Self-interaction correction to density-functional approximations for many-electron systems, Phys. Rev. B **23,** 5048 (1981).

[32] R. D. King-Smith and David Vanderbilt, Theory of polarization of crystalline solids, Phys. Rev. B **47,** 1651 (1993).

[33] D. I. Bilc, R. Orlando, R. Shaltaf, G. M. Rignanese, Jorge Íñiguez, and Ph. Ghosez, Hybrid exchange-correlation functional for accurate prediction of the electronic and

structural properties of ferroelectric oxides, Phys. Rev. B **77,** 1 (2008).

[34] Volker Blum, Ralf Gehrke, Felix Hanke, Paula Havu, Ville Havu, Xinguo Ren, Karsten Reuter, and Matthias Scheffler, Ab initio molecular simulations with numeric atom-centered orbitals, Comput. Phys. Commun. **180,** 2175 (2009).

[35] See Supplemental Material at http://link.aps.org/supple mental/10.1103/PhysRevApplied.13.034066 for information on the structures used to obtain the LDA-to-HSE06 E_g correction, the 80-atom arrangements of 75BTO-25NTM, the binary oxides used in the formation-energy analysis, and data on the CBM, VBM, unit-cell volume, lattice parameters, Born effective charge and piezoelectric properties of the system studied.

[36] Anubhav Jain, Shyue Ping Ong, Geoffroy Hautier, Wei Chen, William Davidson Richards, Stephen Dacek, Shreyas Cholia, Dan Gunter, David Skinner, Gerbrand Ceder, and Kristin A. Persson, The materials project: A materials genome approach to accelerating materials innovation, APL Mater. **1,** 11002 (2013).

[37] Eric Jones, Travis Oliphant, and Pearu Peterson, SciPy: Open source scientific tools for Python, (2001).

[38] Seol Hee Oh, Hae-Young Shin, Seokhyun Yoon, Jai Seok Ahn, Janghwan Cha, Suklyun Hong, Sung Jin Kang, Miyoung Kim, Sukgeun Choi, Changjae Roh, Jongseok Lee, and William Jo, Strain-induced non-linear optical characteristics of pyroelectric $PbVO_3$ epitaxial thin films, Opt. Mater. Express **7,** 62 (2017).

[39] G. Vinai, A. Khare, D. S. Rana, E. Di Gennaro, B. Gobaut, R. Moroni, A. Yu. Petrov, U. Scotti di Uccio, G. Rossi, F. Miletto Granozio, G. Panaccione, and P. Torelli, Unraveling the magnetic properties of $BiFe_{0.5}Cr_{0.5}O_3$ thin films, APL Mater. **3,** 116107 (2015).

[40] Yoonho Ahn and Jong Yeog Son, Epitaxial perovskite Bi_2ZnTiO_6 thin film with high tetragonality, J. Cryst. Growth **433,** 86 (2016).

[41] David Vanderbilt and Morrel H. Cohen, Monoclinic and triclinic phases in higher-order devonshire theory, Phys. Rev. B **63,** 94108 (2001).

[42] F. Detraux, Ph. Ghosez, and X. Gonze, Anomalously large Born effective charges in cubic WO_3, Phys. Rev. B **56,** 983 (1997).

[43] B. P. Burton and E. Cockayne, Why $Pb(B, B')O_3$ perovskites disorder at lower temperatures than $Ba(B, B')_3$ perovskites, Phys. Rev. B **60,** R12542 (1999).